Journal of Solid State Chemistry 182 (2009) 547–554

Contents lists available at ScienceDirect

Journal of Solid State Chemistry

journal homepage: www.elsevier.com/locate/jssc

# Crystal structure of $Eu^{2+}$-doped $M_3MgSi_2O_8$ ($M$: Ba, Sr, Ca) compounds and their emission properties

Yoshinori Yonesaki *, Takahiro Takei, Nobuhiro Kumada, Nobukazu Kinomura

*Interdisciplinary Graduate School of Medical and Engineering, University of Yamanashi, Miyamae 7-32, Kofu 400-8511, Japan*

ARTICLE INFO

*Article history:*
Received 16 September 2008
Received in revised form
17 November 2008
Accepted 22 November 2008
Available online 9 December 2008

*Keywords:*
Divalent europium
Phosphor
Luminescence
Alkali earth magnesium silicate
Crystal structure

ABSTRACT

Emission properties of $Eu^{2+}$-doped $M_3MgSi_2O_8$ ($M$: Ba, Sr, Ca) are discussed in terms of the crystal structure. When $Ba^{2+}$ ions account for over one third of $M^{2+}$ ions, $M_3MgSi_2O_8$ crystallizes in glaserite-type trigonal structure, while Ba-free compounds crystallize in merwinite-type monoclinic structure. Under UV excitation, the $Eu^{2+}$-doped glaserite-type compounds exhibit an intense blue emission assigned to $5d$–$4f$ electron transition at about 435 nm, regardless of the molar ratio of $Ba^{2+}$, $Sr^{2+}$ and $Ca^{2+}$ ions. By contrast, the $Eu^{2+}$-doped merwinite-type compounds show an emission color sensitive to the ratio. A detailed analysis of the emission spectra reveals that the emission chromaticity for the $Eu^{2+}$-doped $M_3MgSi_2O_8$ is composed of two emission peaks reflecting two different sites accommodating $M^{2+}$ ion.



## 1. Introduction

$M_3MgSi_2O_8$ ($M$: Ba, Sr, Ca) compounds have attracted much attention as promising host materials for $Eu^{2+}$-doped blue phosphors. The emission properties have been investigated for improving the intensity and chromaticity [1–7]. Blasse et al. investigated the emission from $Eu^{2+}$ ions doped in the end-members of $M_3MgSi_2O_8$ ternary system ($Ba_3MgSi_2O_8$–$Sr_3MgSi_2O_8$–$Ca_3MgSi_2O_8$), and showed a systematic emission-color shift from blue to green depending on $M^{2+}$-ion size [1]. Barry reported the photoluminescence of $Eu^{2+}$ ions in the solid solutions of $(Ba,Sr)_3MgSi_2O_8$ and $(Sr,Ca)_3MgSi_2O_8$ [2]. According to him, in the $(Ba,Sr)_3MgSi_2O_8$ system, the d-spacing of 222 reflection for an orthorhombic unit cell changed continuously depending on Ba/Sr ratio while the emission wavelength showed discontinuous change at about Ba/Sr = 1. Jung et al. found that $Eu^{2+}$-doped $(Ba,Sr)_3MgSi_2O_8$ exhibited high durability against vacuum ultraviolet irradiation [4]. These results are indicative of its great potential as a blue phosphor replacing $BaMgAl_{10}O_{17}$:$Eu^{2+}$ (BAM). However, their emission properties have been discussed without considering the precise crystal structure or the site substituted by $Eu^{2+}$ ions. The systematic color-shift observed for $M_3MgSi_2O_8$:$Eu^{2+}$ was simply assigned to a geometric distortion caused by $M^{2+}$-ion size supposing that all the compounds had merwinite ($Ca_3MgSi_2O_8$)-type structure (Fig. 1a). In our previous report, it was clarified that $BaCa_2MgSi_2O_8$ crystallized in the trigonal space group $P\bar{3}m1$ (no. 164) and had glaserite ($KNaSO_4$)-type layered structure (Fig. 1b) [7]. The layer is built up by corner-sharing of $MgO_6$ octahedra and $SiO_4$ tetrahedra, and $Ba^{2+}$ and $Ca^{2+}$ ions occupy the distinct interlayer crystallographic sites; $Ba^{2+}$ ion is sited at the center of the interlayer space ($A$-site) and $Ca^{2+}$ ion is embedded in the layer framework ($B$-site). This structure can be regarded as highly-ordered structure of merwinite. The ways of connection among the coordination polyhedra are similar between merwinite-type and glaserite-type structure. However, the layer in the glaserite-type structure is a regular and flat one while that in the merwinite-type structure is corrugated. Then, the $B$-site for the glaserite-type structure separates into two sites ($B'$- and $B''$-sites) in the merwinite-type structure. This structural transition gives rise to the change in coordination number for alkali-earth-metal ions; the interlayer $A$-site cation from 12 in the glaserite-type to 8 in the merwinite-type and the layer-embedded $B$-site cations from 10 to 8 or 9. Under ultraviolet (UV) excitation, $Eu^{2+}$-doped $BaCa_2MgSi_2O_8$ exhibited an intense blue emission which was different from the greenish emission observed for $Eu^{2+}$-doped merwinite. We consider that the chromaticity change among $Eu^{2+}$-doped $M_3MgSi_2O_8$ compounds is partly due to the difference in coordination number for the interlayer sites accompanied by the structural transition as well as the difference in size of the coordination polyhedra caused by the difference in radii of $M^{2+}$ ions. In this study, the emission properties of $M_3MgSi_2O_8$:$Eu^{2+}$ compounds are discussed based on the crystal structure.

* Corresponding author. Fax: +81 55 254 3035.
*E-mail address:* yonesaki@yamanashi.ac.jp (Y. Yonesaki).

0022-4596/$ - see front matter © 2008 Elsevier Inc. All rights reserved.
doi:10.1016/j.jssc.2008.11.032

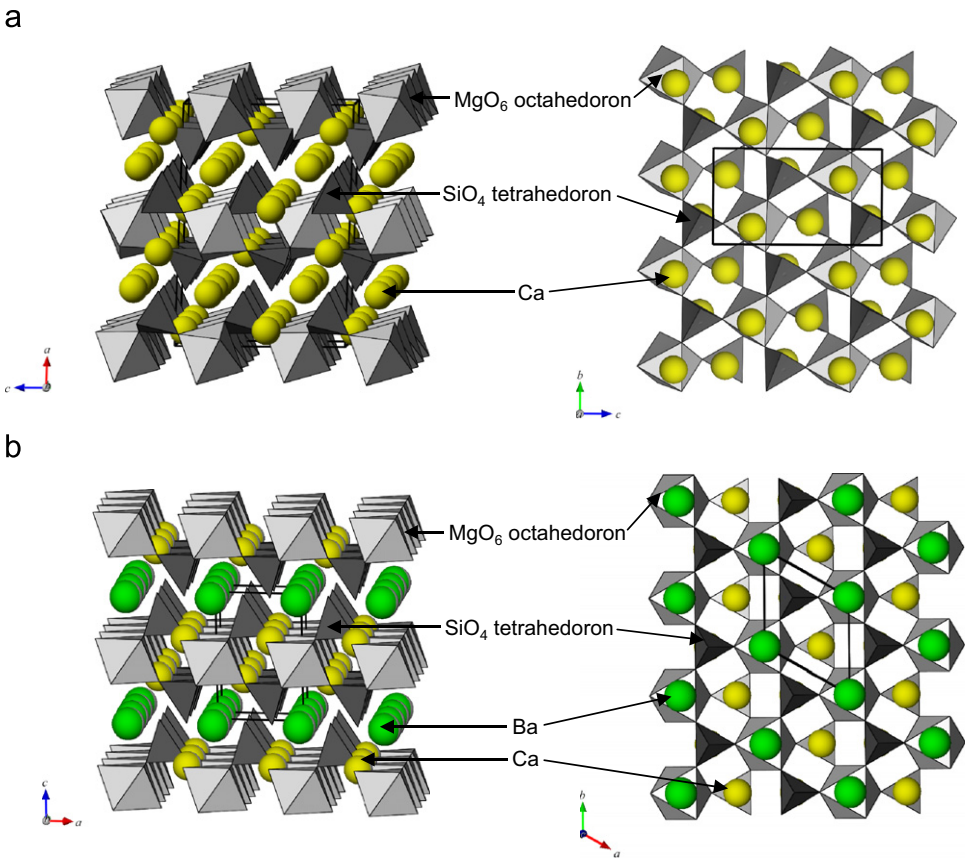


**Fig. 1.** Crystal structure of (a) merwinite ($Ca_3MgSi_2O_8$) and (b) $BaCa_2MgSi_2O_8$ illustrated with $MgO_6$ octahedra and $SiO_4$ tetrahedra. The solid line frame indicates the unit cell of each structure. These figures are quoted from Ref. [7].

## 2. Experimental

### 2.1. Synthesis

Batch compositions investigated in this study are summarized in Table 1, together with their notation. The notation is based on the molar ratio of $Ba^{2+}$, $Sr^{2+}$ and $Ca^{2+}$ for $M^{2+}$ ions. Crystalline powder samples were prepared from reagent grade alkali-earth carbonates, magnesium carbonate hydroxide, silica gel, and $Eu_2O_3$. A small amount of $NH_4Cl$ (about 2 wt%) was used as a flux. Stoichiometric amounts of the reagents and the flux were mixed and ground by ball milling with zirconia beads in 2-propanol for 4 h. The mixed powder was heated at 1100 °C for 4 h in a flow of 2% $H_2$–98% $N_2$ gas with an intermittent re-grinding.

### 2.2. Crystal structure analysis

The prepared samples were investigated by X-ray powder diffraction (XRD) with a Rigaku RINT-2200HFV diffractometer using Cu$K\alpha$ radiation monochromated with graphite ($\lambda = 1.54058$ Å). The structural refinement was carried out with the XRD data collected at intervals of 0.05° or 0.02° from 10° to 120° $2\theta$ at room temperature. Lattice parameters and structure parameters were refined by Rietveld method using a program RIETAN-2000 [8]. Figures of crystal structure in this report were drawn with VICS-II developed by Momma and Izumi.

### 2.3. Characterization of photoluminescent properties

Emission and excitation spectra of the prepared samples were measured at room temperature using a JASCO corporation FP-6500 spectrofluorometer.

**Table 1**
Batch composition of the samples prepared in this study.

| Sample notation | Batch composition in molar ratio |
|---|---|
| 0:0:3 | $Ca_{2.98}Eu_{0.02}MgSi_2O_8$ |
| 0:1:2 | $Sr_{0.98}Eu_{0.02}Ca_2MgSi_2O_8$ |
| 0:2:1 | $Sr_{1.98}Eu_{0.02}CaMgSi_2O_8$ |
| 0:3:0 | $Sr_{2.98}Eu_{0.02}MgSi_2O_8$ |
| 1:0:2 | $BaCa_{1.98}Eu_{0.02}MgSi_2O_8$ |
| 1:1:1 | $Ba_{0.98}Eu_{0.02}SrCaMgSi_2O_8$ |
| 1:2:0 | $Ba_{0.98}Eu_{0.02}Sr_2MgSi_2O_8$ |
| 2:0:1 | $Ba_{1.98}Eu_{0.02}CaMgSi_2O_8$ |
| 2:1:0 | $Ba_{1.98}Eu_{0.02}SrMgSi_2O_8$ |
| 3:0:0 | $Ba_{2.98}Eu_{0.02}MgSi_2O_8$ |

## 3. Results

### 3.1. Crystal structure

The XRD patterns for the prepared samples are shown in Fig. 2. Closed diamonds and triangles indicate the Bragg reflections assigned to $M_3MgSi_2O_8$ crystalline phase with a monoclinic unit cell and a trigonal one, respectively. When $Ba^{2+}$ ion accounts for one third of $M^{2+}$ ions or less, all the reflection peaks are indexed with a monoclinic or a trigonal cell, indicating that the product is single phase. On the other hand, when the amount of $Ba^{2+}$ ion exceeds two thirds, impurities such as $BaMgSiO_4$, $BaMg_2Si_2O_7$ and $\alpha$-$Ca_2SiO_4$ appear in addition to a glaserite-type trigonal phase. Particularly in the 2:0:1 sample, the glaserite-type phases of $BaCa_2MgSi_2O_8$ and $Ba_3MgSi_2O_8$ coexist with the impurities. The discrepancy between the nominal composition and the

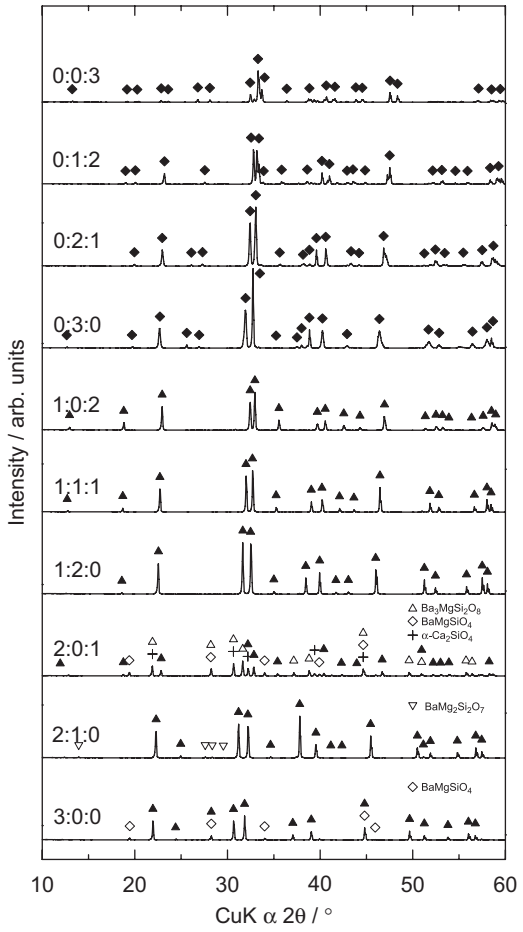


**Fig. 2.** X-ray powder diffraction patterns for the prepared samples. The reflection peaks assigned to the $M_3MgSi_2O_8$ crystalline phase are marked with closed points.

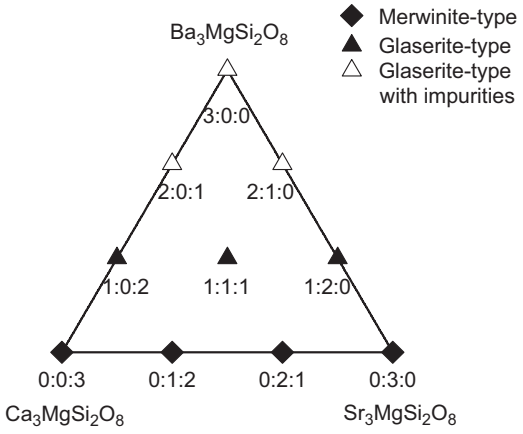


**Fig. 3.** Crystal system of the $M_3MgSi_2O_8$ phase for the prepared samples. Closed points correspond to a single $M_3MgSi_2O_8$ phase and open points to the $M_3MgSi_2O_8$ phases appeared with some impurities.

synthesized $M_3MgSi_2O_8$ phases is discussed later in association with $M_3MgSi_2O_8$ crystal structure. Fig. 3 shows the structure type of the $M_3MgSi_2O_8$ phase synthesized from each sample. Closed diamonds and triangles correspond to the appearance of a merwinite-type phase and a glaserite-type phase, respectively. Open triangles indicate the appearance of glaserite-type phases together with some impurities. It is worth noting that, after XRD measurements, the 3:0:0 and 2:0:1 samples show irreversible discoloration from original white to reddish orange at the X-ray irradiated area (Fig. 4). When as-prepared 3:0:0 sample was illuminated with a low-pressure mercury vapor UV lamp, similar discoloration, which was possibly due to the change in ligand field for $Eu^{2+}$ ions, was observed. Furthermore, deterioration of the XRD peaks was seen for the 3:0:0 sample after the repeated XRD measurements. These results implied that the glaserite-type $Ba_3MgSi_2O_8$ phase was instable against short-wavelength radiation. The discoloration observed for the 2:0:1 sample probably came from the $Ba_3MgSi_2O_8$ phase in the product.

Based on the monoclinic structure model of merwinite ($Ca_3MgSi_2O_8$, Fig. 1a) [6] or the trigonal structure model of glaserite ($KNaSO_4$, Fig. 1b) [9], crystal structure of the $M_3MgSi_2O_8$ phases was successfully refined on the assumption that each site for $M^{2+}$ ion was occupied by mixed alkali-earth metal ions. For

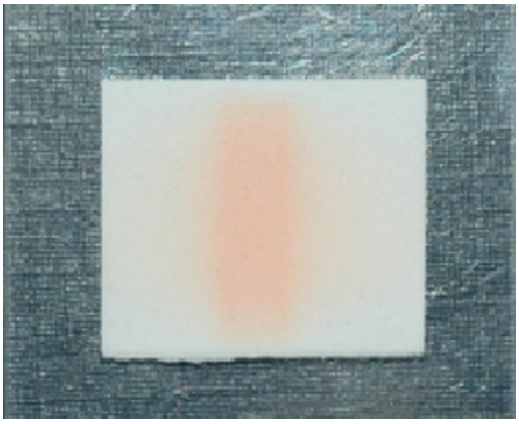

**Fig. 4.** Photograph of the 3:0:0 sample after Cu$K\alpha$ X-ray irradiation (center part).

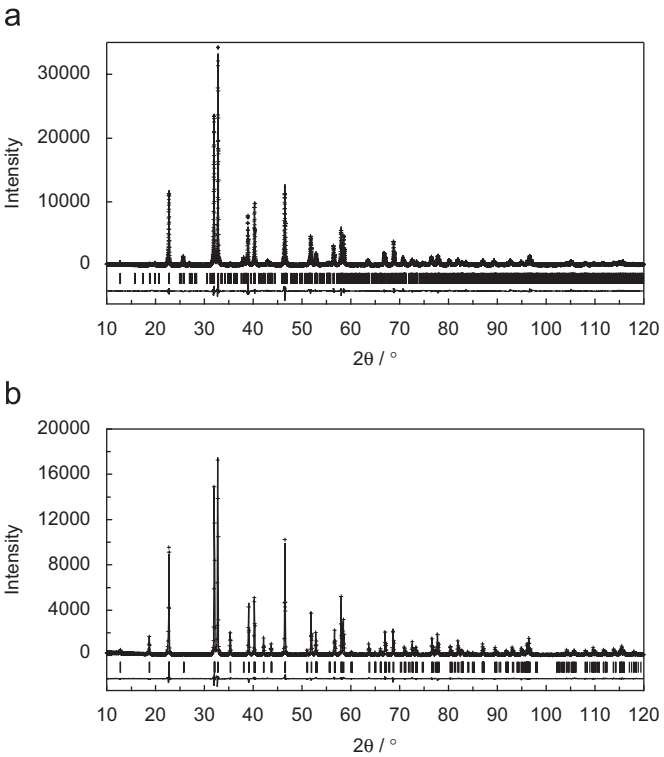


**Fig. 5.** Observed and calculated X-ray powder diffraction patterns for (a) 0:3:0 and (b) 1:1:1 samples. Solid line is the calculated pattern from the refined crystal structure. Residual errors are drawn at the bottom of the figure. Vertical short lines are allowed peak positions satisfying Bragg condition.

easy comparison with glaserite-type structure, $P2_1/a$ (the third setting of the space group no. 14) was selected for the merwinite-type phase. Although the 0:1:2 sample exceptionally crystallized in the monoclinic space-group $A2$ (the second setting of the space group no. 5), it was also found to have merwinite-like layered structure. Fig. 5 shows the Rietveld refinement patterns for $Sr_{2.98}Eu_{0.02}MgSi_2O_8$ (0:3:0 sample) and $Ba_{0.98}Eu_{0.02}SrCaMgSi_2O_8$ (1:1:1 sample) as a representative for each structure type. Lattice parameters and structure parameters for them are listed in Tables 2 and 3. Lattice constants for all the $M_3MgSi_2O_8$ phases are listed in Table 4. The occupancy of $Ba^{2+}$, $Sr^{2+}$ and $Ca^{2+}$ ions for $A$-, $B$- ($B'$- and $B''$-) site solved by the refinement process is summarized in Table 5. As seen in this table, when more than two kinds of alkali-earth metal ions are included in the structure, a large ion tends to occupy the interlayer $A$-site and a small ion the sites related to the $B$-site. The lattice constants and unit cell volumes are plotted against the summation of radii of the alkali-earth-metal ions occupying each site with diamonds for merwintie-type monoclinic structure and with triangles for glaserite-type trigonal structure in Figs. 6 and 7, respectively. Here, the ionic radius is defined as the summation of Shannon's ionic radius [10] multiplied by occupancy for relevant $M^{2+}$ ions. Lattice constants for the trigonal phases are converted to those for the corresponding monoclinic phases with the relation that $a_m = 2c_t$, $b_m = a_t$ and $c_m = \sqrt{3}a_t$ (subscript "m" means monoclinic and "t" trigonal). In Figs. 8 and 9, $(a_m \sin\beta)/2$, a measure of the layer-stacking period,

**Table 2**
Crystallographic data for $Sr_{2.98}Eu_{0.02}MgSi_2O_8$ for 0:3:0 sample and $Ba_{0.98}Eu_{0.02}SrCaMgSi_2O_8$ for 1:1:1 sample.

| | 0:3:0 | 1:1:1 |
|---|---|---|
| Empirical formula | $Sr_3MgSi_2O_8$ | $BaSrCaMgSi_2O_8$ |
| Formula weight | 471.33 | 473.49 |
| Crystal system, space group | Monoclinic, $P2_1/a$ (no. 14) | Trigonal, $P\bar{3}m1$ (no. 164) |
| Unit cell parameters | $a = 13.877(2)$ Å<br>$b = 5.4577(8)$ Å<br>$c = 9.452(14)$ Å<br>$\beta = 90.000(7)^\circ$ | $a = 5.4647(8)$ Å<br>$c = 6.9105(7)$ Å |
| Volume (Å$^3$) | 715.9(18) | 178.72(4) |
| $Z$ | 4 | 1 |
| Calculated density (g/cm$^3$) | 4.37 | 4.40 |
| Goodness of fit | 2.68 | 1.55 |
| $R_p$ (%) | 9.52 | 7.00 |
| $R_{wp}$ (%) | 13.53 | 9.71 |
| $R_I$ (%) | 2.07 | 1.23 |
| $R_F$ (%) | 1.47 | 0.57 |

**Table 3**
(a) Atomic coordinates and isotropic displacement parameteres for $Sr_{2.98}Eu_{0.02}MgSi_2O_8$ and (b) atomic coordinates and isotropic displacement parameters for $Ba_{0.98}Eu_{0.02}SrCaMgSi_2O_8$.

| Atom | Site | $g$ | $x$ | $y$ | $z$ | $B_{iso}$ (Å$^2$) |
|---|---|---|---|---|---|---|
| (a) | | | | | | |
| Sr1 | 4*e* | 1 | 0.2500(4) | 0.2126(4) | 0.2528(5) | 1.75(7) |
| Sr2 | 4*e* | 1 | 0.0862(2) | 0.246(10) | 0.9189(8) | 1.0(10) |
| Sr3 | 4*e* | 1 | 0.0889(2) | 0.741(10) | 0.4230(7) | 0.72(9) |
| Mg | 4*e* | 1 | −0.003(11) | 0.235(3) | 0.247(15) | 0.5(16) |
| Si1 | 4*e* | 1 | 0.1407(6) | 0.253(3) | 0.574(19) | 0.50(9) |
| Si2 | 4*e* | 1 | 0.1300(7) | 0.739(3) | 0.082(2) | = $B_{iso}$(Si1) |
| O1 | 4*e* | 1 | 0.087(18) | 0.255(5) | 0.428(2) | 0.6(15) |
| O2 | 4*e* | 1 | 0.073(15) | 0.459(5) | 0.680(3) | = $B_{iso}$(O1) |
| O3 | 4*e* | 1 | 0.085(16) | 0.999(5) | 0.655(3) | = $B_{iso}$(O1) |
| O4 | 4*e* | 1 | 0.241(16) | 0.287(6) | 0.560(3) | 2.9(3) |
| O5 | 4*e* | 1 | 0.125(14) | 0.737(5) | 0.925(2) | = $B_{iso}$(O1) |
| O6 | 4*e* | 1 | 0.250(16) | 0.764(5) | 0.085(4) | = $B_{iso}$(O4) |
| O7 | 4*e* | 1 | 0.107(14) | 0.462(4) | 0.181(3) | = $B_{iso}$(O1) |
| O8 | 4*e* | 1 | 0.077(14) | 0.936(4) | 0.167(3) | = $B_{iso}$(O1) |
| (b) | | | | | | |
| Ba1 | 1*a* | 0.94(5) | 0 | 0 | 0 | 0.67(4) |
| Sr1 | 1*a* | = 1–2 g(Sr2) | = $x$(Ba1) | = $y$(Ba1) | = $z$(Ba1) | = $B_{iso}$(Ba1) |
| Ca1 | 1*a* | = 1–g(Ba1)-g(Sr1) | = $x$(Ba1) | = $y$(Ba1) | = $z$(Ba1) | = $B_{iso}$(Ba1) |
| Ba2 | 2*d* | = [1–g(Ba1)]/2 | 2/3 | 1/3 | 0.6600(3) | 0.53(6) |
| Sr2 | 2*d* | 0.48(6) | = $x$(Ba2) | = $y$(Ba2) | = $z$(Ba2) | = $B_{iso}$(Ba2) |
| Ca2 | 2*d* | = 1–g(Ba2)-g(Sr2) | = $x$(Ba2) | = $y$(Ba2) | = $z$(Ba2) | = $B_{iso}$(Ba2) |
| Mg | 1*b* | 1 | 0 | 0 | 1/2 | 0.5(14) |
| Si | 2*d* | 1 | 2/3 | 1/3 | 0.2253(6) | 0.35(8) |
| O1 | 2*d* | 1 | 2/3 | 1/3 | 0.001(16) | 1.2(18) |
| O2 | 6*i* | 1 | 0.1779(6) | = 2$x$(O2) | 0.6766(9) | 1.6(12) |

**Table 4**
Crystallographic data for $M_3MgSi_2O_8$.

| Sample | 0:0:3 | 0:1:2 | 0:2:1 | 0:3:0 | 1:0:2 | 1:1:1 | 1:2:0 | 2:1:0 | 3:0:0 |
|---|---|---|---|---|---|---|---|---|---|
| C.S., S.G. | Monoclinic, $P2_1/a$ | Monoclinic, $A2$ | Monoclinic, $P2_1/a$ | Monoclinic, $P2_1/a$ | Trigonal, $P\bar{3}m1$ | Trigonal, $P\bar{3}m1$ | Trigonal, $P\bar{3}m1$ | Trigonal, $P\bar{3}m1$ | Trigonal, $P\bar{3}m1$ |
| Unit cell parameters | $a_m = 13.296(3)$ Å<br>$b_m = 5.308(12)$ Å<br>$c_m = 9.346(2)$ Å<br>$\beta = 92.047(14)^\circ$ | $a_m = 13.415(2)$ Å<br>$b_m = 5.349(10)$ Å<br>$c_m = 9.345(17)$ Å<br>$\beta = 90.0668(9)^\circ$ | $a_m = 13.647(3)$ Å<br>$b_m = 5.432(10)$ Å<br>$c_m = 9.367(18)$ Å<br>$\beta = 90.2606(7)^\circ$ | $a_m = 13.877(2)$ Å<br>$b_m = 5.4577(8)$ Å<br>$c_m = 9.452(14)$ Å<br>$\beta = 90.000(7)^\circ$ | $a_t = 5.428(14)$ Å<br>$c_t = 6.802(13)$ Å | $a_t = 5.4647(8)$ Å<br>$c_t = 6.9105(7)$ Å | $a_t = 5.4972(4)$ Å<br>$c_t = 7.0131(4)$ Å | $a_t = 5.5515(6)$ Å<br>$c_t = 7.1402(5)$ Å | $a_t = 5.6083(10)$ Å<br>$c_t = 7.2652(14)$ Å |
| Volume (Å$^3$) | 659.3(3) | 670.6(2) | 694.5(2) | 715.9(18) | 173.59(7) | 178.72(4) | 183.53(2) | 190.57(3) | 197.905(6) |
| $Z$ | 4 | 4 | 4 | 4 | 1 | 1 | 1 | 1 | 1 |
| Calculated density (g/cm$^3$) | 3.38 | 3.73 | 4.05 | 4.37 | 4.07 | 4.40 | 4.71 | 4.97 | 5.21 |

Subscripts "t" and "m" written as subscripts to the right of lattice parameter mean trigonal and monoclinic system, respectively.

is plotted against the average size of alkali-earth-metal ions at *A*- and *B*- (*B*′- and *B*″-) site, respectively. From these figures, it is found that interlayer distance linearly correlates with average size of layer-embedded ions.

### 3.2. Photoluminescent properties

The prepared samples exhibited intense emissions under 254-nm excitation. As seen in Fig. 10, the prepared samples show broad emission peaks derived from 5*d*-4*f* electron transition in divalent europium ions. Because the 2:0:1 sample contains two

**Table 5**
Occupancy for each site accommodating $M^{2+}$ ion.

| | A-site | | | *B*-site (*B*′-site) | | | *B*″-site | | |
|---|---|---|---|---|---|---|---|---|---|
| | Ba | Sr | Ca | Ba | Sr | Ca | Ba | Sr | Ca |
| 0:0:3 | – | – | 1 | – | – | 1 | – | – | 1 |
| 0:1:2 | – | 0.72 | 0.28 | – | 0.141 | 0.859 | – | 0.141 | 0.859 |
| 0:2:1 | – | 1 | – | – | 0.47(11) | 0.52 | – | 0.52 | 0.47 |
| 0:3:0 | – | 1 | – | – | 1 | – | – | 1 | – |
| 1:0:2 | 0.947(5) | – | 0.053 | 0.02 | – | 0.973 | | | |
| 1:1:1 | 0.94(5) | 0.02 | 0.02 | 0.02 | 0.48(5) | 0.48 | | | |
| 1:2:0 | 0.825(7) | 0.174 | – | 0.087 | 0.912 | – | | | |
| 2:1:0 | 0.86(11) | 0.13 | – | 0.56 | 0.43 | – | | | |
| 3:0:0 | 1 | – | – | 1 | – | – | | | |

Occupancy ratio refined was denoted with the standard deviation.

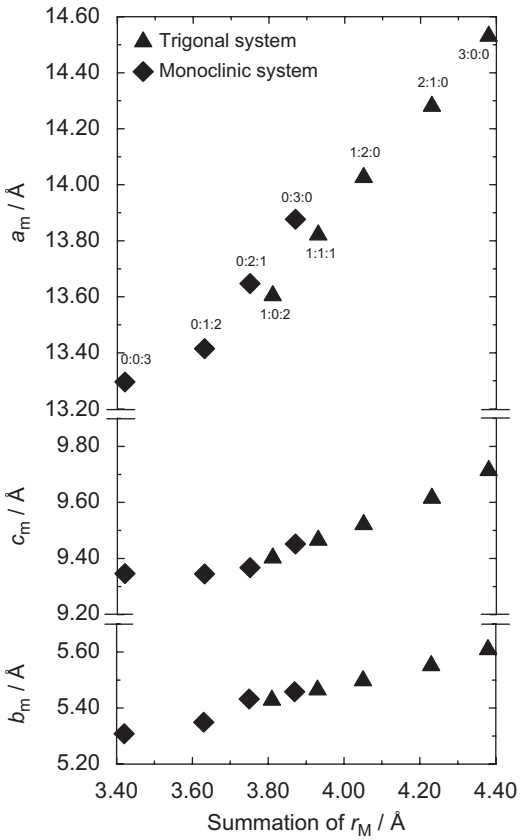


**Fig. 6.** Dependence of the lattice constants for $M_3MgSi_2O_8$ phase on the summation of the radii of alkali-earth-metal ions occupying three *M*-sites ($r_M$). Lattice constants for the glaserite-type compounds are converted to those for the corresponding monoclinic cell. Diamond and triangle plots represent the data for monoclinic and trigonal phases, respectively.

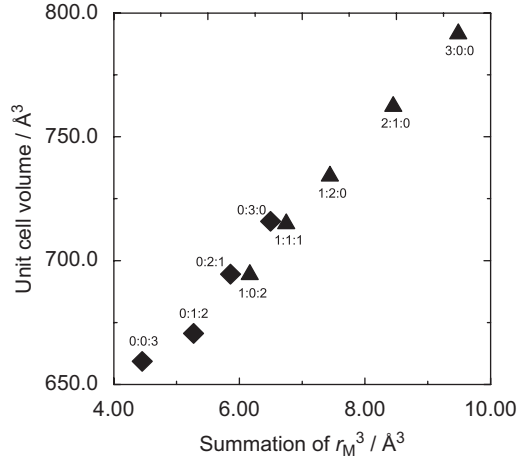


**Fig. 7.** Unit cell volume of $M_3MgSi_2O_8$ phase plotted against the summation of cubed ionic radii for the alkali-earth-metal ions at three *M*-sites. Diamond and triangle plots represent the data for monoclinic and trigonal phase, respectively.

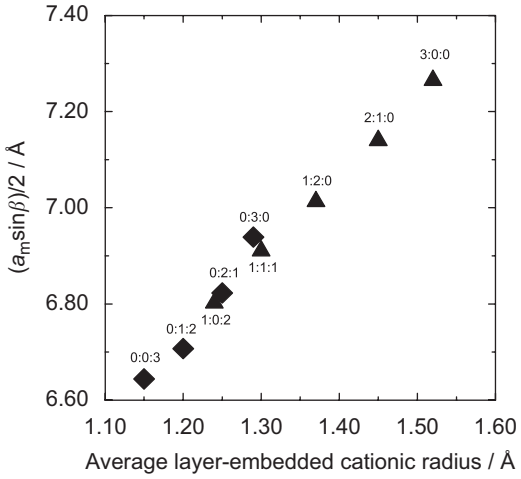


**Fig. 8.** Period of unit-layer stacking for $M_3MgSi_2O_8$ phase plotted against average radius of the layer-embedded cations. Diamond and triangle plots represent the data for monoclinic and trigonal dominant phase, respectively.

glaserite-type phases, its photoluminescent properties are not discussed here. The emission peak is apt to broaden with an increase in small alkali-earth-metal ions. Particularly, the addition of $Ca^{2+}$ ions results in asymmetric broadening to longer wavelength side. The glaserite-type compounds (Ba-containing samples) show similar emission-peak wavelengths and chromaticity while those for the merwinite-type compounds depend on nominal Sr-content. Fig. 11 shows emission- and excitation-wavelength dependence of the emission intensity normalized with the peak-top value. It is found from the figure that the spectra can be divided into two types according to emission-peak form. Compared with the 0:0:3, 0:1:2, 0:2:1 and 0:3:0 samples, the 1:0:2, 1:1:1, 1:2:0, 2:1:0 and 3:0:0 samples exhibit emission peaks at shorter wavelength, and the efficient excitation-wavelength ranges are narrower. Interestingly, this classification is completely coincided with that based on the crystal structure; merwinite-type or glaserite-type. Regarding the merwinite-type compounds, it is obvious that excitation spectrum suddenly changes the shape at about 455-nm emission wavelength (Fig. 11), which indicates that the emission spectra are composed of two emission peaks; one has a peak at 455 nm, and the other at

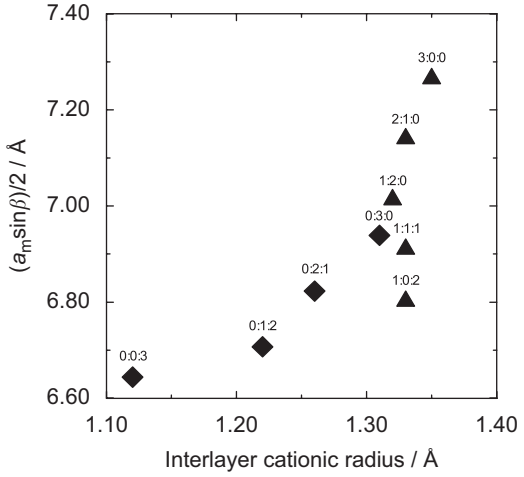


**Fig. 9.** Period of unit-layer stacking for $M_3MgSi_2O_8$ phase against radius of the interlayer cation. Diamond and triangle plots represent the data for monoclinic and trigonal phase, respectively.

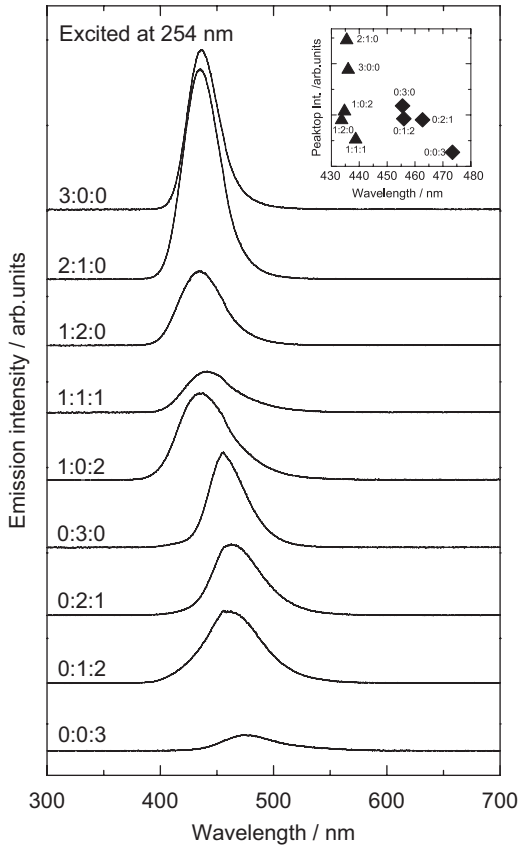


**Fig. 10.** Emission spectra for the prepared samples under 254-nm excitation. The inset shows the intensity and wavelength of the emission peak-top.

a longer wavelength. The chromaticity shift seen in the spectrum comes from the two emission components. The 455-nm peak is observed only for Sr-containing compounds and does not show significant shift against nominal $M^{2+}$ ratio. In contrast, the longer-wavelength emission peak which is recognized only for Ca-containing compounds shows blue-shift with an increase in nominal Sr-content. These results show that $Eu^{2+}$ ions occupy two different sites, at one of which crystal field changes depending on nominal Sr-content.

## 4. Discussion

### 4.1. Crystal structure

$M_3MgSi_2O_8$ has layered structure either monoclinic merwinite-type (Fig. 1a) or trigonal glaserite-type (Fig. 1b). Corner-sharing $MgO_6$ octahedra and $SiO_4$ tetrahedra are polymerized to form the layer [7,9]. Between the layers, there are three sites for alkali-earth-metal ions; one is at the center of the interlayer space (*A*-site) and the remaining two are embedded in the layer (*B*′- and *B*″-sites). In glaserite-type structure, *B*′- and *B*″-sites are crystallographically identical (*B*-site). As mentioned above, the glaserite-type structure is regarded as highly ordered structure of merwinite-type. Despite the difference of the structure type, the unit cell volumes of merwinite-type compounds and those of glaserite-type compounds which are converted to merwinite-type cell almost lie on a line against the summation of cubed radii for $M^{2+}$ ions (Fig. 7). Here, the glaserite-type structure is featured in Fig. 12. It is worthwhile to mention that the distance between O1 and *B*-site ion is extraordinarily short compared with that predicted from Shannon's ionic radii [7]. We may say that the layers are supported by the Si–O1–B bond and hence the interlayer distance linearly depends on the size of $M^{2+}$ ion at the layer-embedded sites (Fig. 8). On the other hand, the room where a large *A*-site ion locates is limited by *A*–O1 distance in lateral direction and by the distance between $MgO_6$ octahedra on upper and lower layers (summation of a $SiO_4$ tetrahedron and the size of *B*-site ion) in vertical direction. From the results of the structural refinement, *A*–O1 distance in the glaserite-type phases prepared in this study was found to be at least 3.13 Å (calculated from the refined glaserite-type structure of the 1:0:2 sample), which is much longer than the *A*–O distance estimated from Shannon's ionic radii [10] even under the assumption that the largest $Ba^{2+}$ ion occupies *A*-site. If $Sr^{2+}$ or $Ca^{2+}$ ion occupies *A*-site, a large estrangement occurs especially in lateral direction. Hence, the deformation from glaserite-type to merwinite-type is considered to occur to eliminate the large estrangement in Ba-free samples.

In glaserite-type structure, large $M^{2+}$ ion tends to occupy *A*-site as well as in merwinite-type structure (Table 5). However, when the amount of $Ba^{2+}$ exceeds one-third of $M^{2+}$ ions, a part of $Ba^{2+}$ ions inevitably resides at *B*-site which is suitable for small ion. This situation may cause the instability of the glaserite-type compounds rich in $Ba^{2+}$ ions. In fact, in the composition region of $Ba^{2+} > 1/3$ of $M^{2+}$, products always contain impurity phases. In the extreme case of the 3:0:0 sample, the discoloration accompanied by the destruction of $Ba_3MgSi_2O_8$ phase is observed on the irradiation of UV and X-ray (Fig. 4). As seen in Fig. 2, the 2:0:1 sample contains two glaserite phases ($BaCa_2MgSi_2O_8$ and $Ba_3MgSi_2O_8$) and impurities. These results suggest that $Ba^{2+}$-occupation for *B*-site destabilizes the glaserite-type structure. The structural refinement also revealed that in merwinite-type structure, there is no distinct difference in coordination number among the three sites accommodating $M^{2+}$ ion (eight- or ninefold coordination).

### 4.2. Photoluminescent properties

#### 4.2.1. Merwinite-type compounds

Generally, the peak wavelength of the emission originated in 5*d*–4*f* electron transition strongly depends on the crystal-field experienced by $Eu^{2+}$ ions. Since the coordination number is not so different among *A*-, *B*′- and *B*″-sites in merwinite-type structure, the distance between $M^{2+}$ ion and ligand oxide ions is the main factor affecting the crystal-field. Because Sr/Ca occupancy for *A*-site differs little (Table 5), the crystal-field for *A*-site ion is nearly equivalent among all the Sr-containing merwinite-type

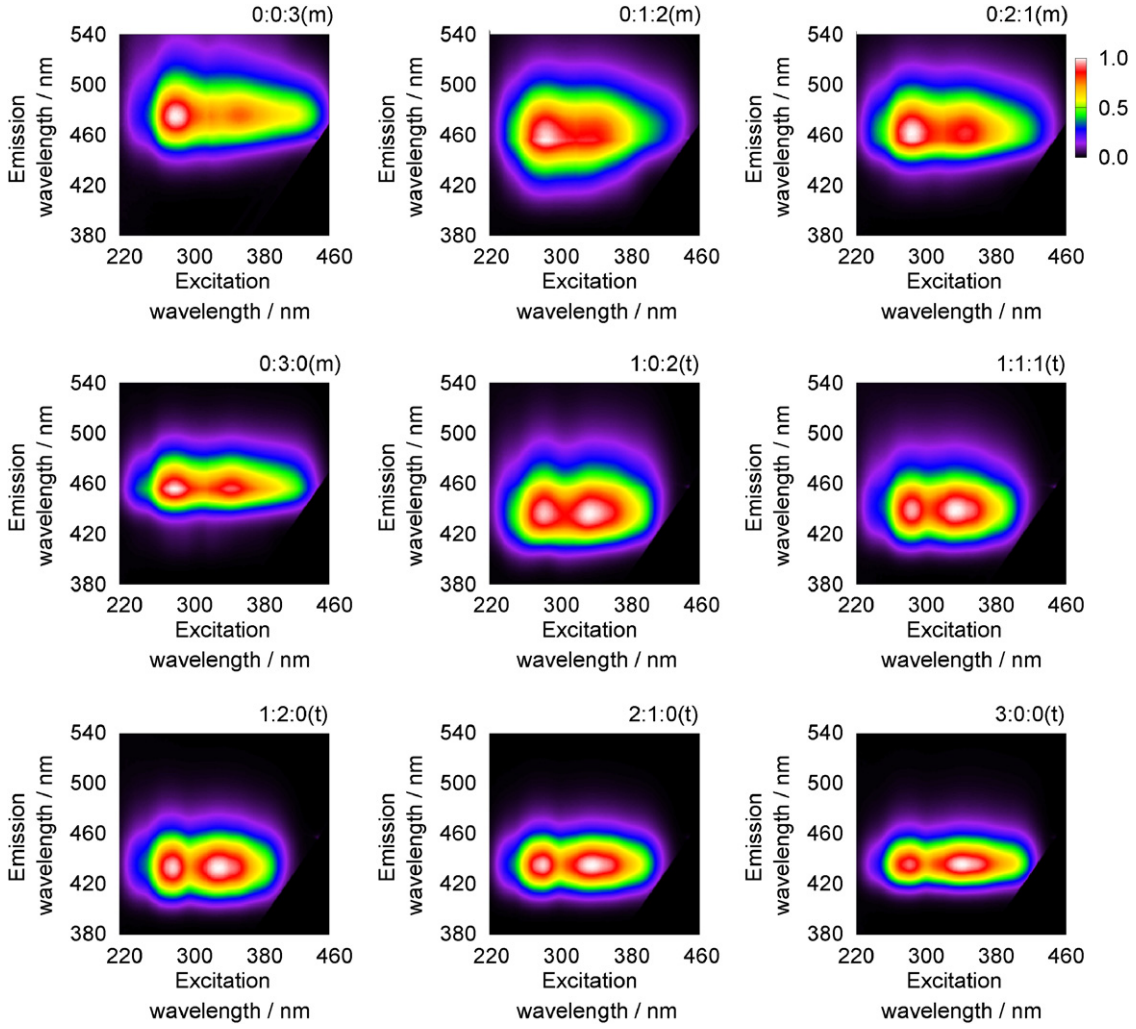


**Fig. 11.** Excitation- and emission-wavelength dependence of the emission intensity normalized with the peak-top value. The crystal system of the $M_3MgSi_2O_8$ phase is shown by (m) for monoclinic merwinite-type and (t) for trigonal glaserite-type.

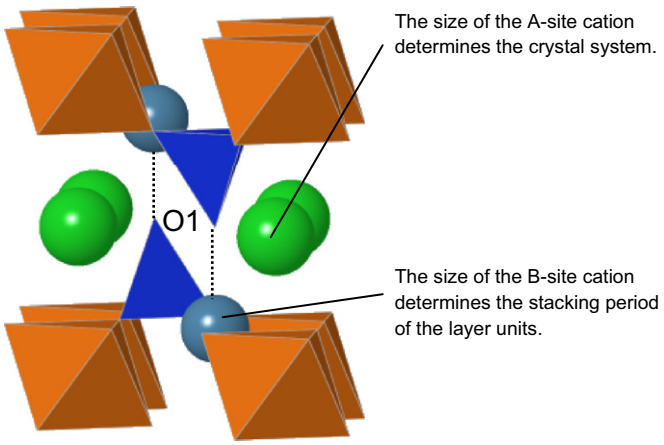


**Fig. 12.** Relationship between crystal structure and alkali-earth-metal ion occupying each site.

compounds. It means that $Eu^{2+}$ ions placed at *A*-site show an emission peak at a certain wavelength, regardless of nominal Sr-content. In contrast, Sr-occupancy for the layer-embedded (*B′*- and *B″*-) sites systematically increases with increasing Sr-content. Since the rise in Sr-occupancy causes the enlargement of the coordination polyhedra and subsequent weakening of the crystal-field, the emission from the $Eu^{2+}$ ions occupying these sites shows blue-shift with an increase in Sr-content. Thus, it is speculated that the emission peak at 455 nm corresponds to the $Eu^{2+}$ ions at *A*-site, and that at a longer wavelength to the $Eu^{2+}$ ions at *B′*- or *B″*-sites. As for the 0:0:3 sample, because all the site for $M^{2+}$ ion are occupied by $Ca^{2+}$ ion, the coordination environment for *A*-site ion is similar with those at *B′*- and *B″*-sites. Therefore, the emission peak at 455 nm disappears (Figs. 11 and 12).

### 4.2.2. *Glaserite-type compounds*

It is reported that the emission from $Eu^{2+}$-doped $BaCa_2MgSi_2O_8$ is characterized by an intense emission at 430.4 nm originated from $Eu^{2+}$ ions at *B*-site (*Ca*-site) and a weak emission at about 450 nm originated from $Eu^{2+}$ ions at *A*-site (*Ba*-site) [7]. The existence of the two emission components is suggested also for other glaserite-type compounds from the result that Ca-addition causes asymmetric broadening of the whole emission peak to longer-wavelength side (Figs. 10 and 11). Based on Ref. [7], the asymmetric broadening can be explained from $M^{2+}$-ion size. As described in the previous section, small alkali-earth-metal ions are prone to be at *B*-site. Hence, $Ca^{2+}$ ions preferentially occupy *B*-site, if exist. However, the site accommodating only $Ca^{2+}$ ion is small for $Eu^{2+}$ ion. As a result, a part of doped $Eu^{2+}$ ions is excluded

from *B*-site, and occupies *A*-site, leading to the second emission peak at a longer wavelength. In Ca-free samples, *A*-site-derived emission peak is not recognizable. It is possibly due to the fact that the unit layer which is laterally expanded by $Sr^{2+}$ or $Ba^{2+}$ ions at *B*-site inhibit the exclusion of $Eu^{2+}$ ion from *B*-site to *A*-site.

Barry pointed out about the emission of $M_3MgSi_2O_8$:$Eu^{2+}$ that the emission color became least sensitive when the dominant alkali-earth-metal ion is larger than $Eu^{2+}$ ion, and most sensitive when it is as small as $Ca^{2+}$ ion [2]. This trend is also confirmed in the present study. The discussion so far clarifies that the trend is attributable to the difference in crystal structure. A fine change in emission chromaticity is induced by $Eu^{2+}$ distribution between the interlayer site and the layer-embedded site for glaserite-type compounds and by the expansion of the coordination polyhedra around the layer-embedded site for merwinite-type phases.

## 5. Conclusion

The layered structure of $M_3MgSi_2O_8$ is discussed focusing on the alkali-earth-metal ions ($M^{2+}$ ions). $M_3MgSi_2O_8$ crystalline phase can have a trigonal form of glaserite-type structure or a monoclinic form of merwinite-type structure. The crystal system is determined by the largest alkali-earth-metal ion occupying the interlayer *A*-site. By contrast, small alkali-earth-metal ions are prone to be at the layer-embedded *B*-site. They play an important role in determining the layer-stacking period.

$Eu^{2+}$-doped $M_3MgSi_2O_8$ exhibits an intense emission. The chromaticity is closely related with the crystal structure. The glaserite-type compounds show an emission peak at a certain wavelength, independent of $M^{2+}$ ions. On the other hand, in merwinite-type compounds, emission chromaticity changes in response to Sr-occupancy for the layer-embedded sites.

## References

[1] G. Blasse, W.L. Wanmaker, J.W. Vrugt, A. Bril, Philips Res. Rep. 23 (1968) 189–200.
[2] T.L. Barry, J. Electrochem. Soc. 115 (1968) 733–738.
[3] J.S. Kim, P.E. Jeon, J.C. Choi, H.L. Park, S.I. Mho, G.C. Kim, Appl. Phys. Lett. 84 (2004) 2931–2933.
[4] H.K. Jung, K.S. Seo, Opt. Mater. 28 (2006) 602–605.
[5] J.S. Kim, A.K. Kwon, Y.H. Park, J.C. Choi, H.L. Park, G.C. Kim, J. Lumin. 122–123 (2007) 583–586.
[6] Y. Lin, Z. Zhang, Z. Tang, X. Wang, J. Zhang, Z. Zheng, J. Eur. Ceram. Soc. 21 (2001) 683–685.
[7] Y. Yonesaki, T. Takei, N. Kumada, N. Kinomura, J. Lumin. 128 (2008) 1507–1514.
[8] F. Izumi, T. Ikeda, Mater. Sci. Forum 321–324 (2000) 198–203.
[9] P.B. Moore, T. Araki, Am. Mineral. 57 (1972) 1355–1374.
[10] R.D. Shannon, Acta Crystallogr. A 32 (1976) 751–767.